PAPER

Visible-light photocatalysis on C-doped ZnO derived from polymer-assisted pyrolysis†

Ahmad S. Alshammari,*[a] Lina Chi,[bc] Xiaoping Chen,[bc] Abdulaziz Bagabas,[a] Denis Kramer,[b] Abdulaziz Alromaeh[a] and Zheng Jiang*[b]

C-doped ZnO with a large surface area was prepared *via* F127-assisted pyrolysis at 500 °C and used for visible-light-responsive photocatalytic water purification. The band structure of the C-doped ZnO was investigated using valance band XPS and DFT simulation. The C-doped ZnO possessed enhanced absorption of UV and visible light, though it showed lower visible-light-responsive photocatalytic activity than ZnO because of significant recombination of photogenerated charge carriers arising from overloaded C-dopant and oxygen vacancies.

1. Introduction

Solar energy photocatalysis on heterogeneous photocatalysts is a promising sustainable process for environment remediation and artificial photosynthesis, while its viability in practice highly depends on effective photocatalysts.[1–4] Among various photocatalysts, ZnO and TiO₂ are most plausible due to their high photosensitivity, nontoxicity, low cost, though they can only utilise a small portion of solar energy (3–5%) in the UV region owing to their large bandgap.[5–8] Similar to TiO₂, ZnO possesses great potential in modulation of bandgap for harvesting visible light but it is easier to crystallise and use in the manufacture of devices.[5,9,10] The bandgap of ZnO may be tuned *via* doping with non-metal or transition metal, or hybridising with other small-bandgap semiconductor or metal to form Shockley junctions, or creating structural vacancies.[1,5,11,12] Motivated by the success in the enhanced visible-light response of non-metal-doped TiO₂, non-metal-doped ZnO photocatalysts have been extensively attempted because the non-metal (S, N or C) dopants can extend visible light absorption significantly and well suppress photogenerated charge recombination at suitable doping level.[7,9,13–19]

C-doped ZnO is an emerging visible-light-responsive photocatalyst with desirable performance in cleaning up

waste water, water splitting and photoelectrochemical cells.[7–9,11,20] Although synthesis of C-doped ZnO represents a considerable challenge, a few methodologies have been successfully established, including self-doping *via* thermal decomposition of $Zn_5(CO_3)_2(OH)_6$ precursor,[7] pyrolysis of Zn-containing inorganic–organic presursors,[8,14] polymer or carbon templated syntheses,[9] metal organic chemical vapour deposition (MOCVD)[21] and thermal plasma in-flight carbonisation techniques.[22] The polymer-assisted pyrolysis synthesis allows incorporation carbon into ZnO matrix and improving its porosity.[8,14] However, different C-doping species or multi-level oxygen vacancies (O_{vac}) would co-existed in the resultant C-doped ZnO materials,[7,23] resulting in the difficulty to clarify their origin of visible-light response, so did C-doped TiO₂.[16,18,19] In principle, light C-doping may extend visible-light absorption and promote their visible-light-driven photocatalysis,[8,12,23,24] while heavy C-doping is highly possible to cause recombination of photogenerated charge carriers. Therefore, it is essential to investigate the roles of C-dopant and O_{vac} in the harvesting visible-light and visible-light-responsive photocatalysis for C-doped ZnO with heavy C-doping level.

In this study, Pluronic F127 ($EO_{106}PO_{70}EO_{106}$) copolymer was adopted for incorporating carbon into ZnO and improves its porosity through a polymer-assisted thermal pyrolysis at 500 °C. The crystal phase, morphology, porosity, light absorption properties and carbon species of the received C-doped ZnO were carefully characterised. The origin of the visible-light response of the C-doped ZnO was interpreted *via* valance band XPS and first-principle simulation using CASTEP package. The photocatalysis performance of ZnO and C-doped ZnO was comparatively evaluated under visible-light to conclude the roles of C-doping.

[a]*National Nanotechnology Research Center, King Abdulaziz City for Science and Technology, King Abdullah Road, P.O. Box 6086, Riyadh 11442, Saudi Arabia. E-mail: aalshammari@kacst.edu.sa; Tel: +966 011 481 4285*

[b]*Faculty of Engineering and The Environment, University of Southampton, Southampton, SO17 1BJ, UK. E-mail: z.jiang@soton.ac.uk; Tel: +44 (0) 2380594893*

[c]*School of Environmental Science and Engineering, Shanghai Jiao Tong University, Shanghai, 200240, China*

† Electronic supplementary information (ESI) available: Fig. S1 PDOS of (a) O and (b) Zn in Wurtzite ZnO crystal; Fig. S2, Methylene Blue Photodegradation over ZnO and C-doped ZnO with different C-doping levels. See DOI: 10.1039/c4ra17227b

2. Experimental and computational

2.1 Sample preparation

All the chemicals were of reagent-grade and were used as purchased from Sigma-Aldrich Company without further purification. Deionized water was used in all experiments.

In the synthesis of C-doped ZnO, 5.9 g of $Zn(NO_3)_2 \cdot 6H_2O$ was dissolved in 50 ml of mixed solution of deionized water and ethanol (water–ethanol = 1 : 1 in volume ratio) to form a clear solution, then 0.75 g of F127 was added. The resulting mixed solution was moved into an electric oven at 90 °C and heated overnight to vapour solvents and form dry polymer metal–organic complex. The dry complex was calcined in muffle furnace up to 500 °C for 3 hours in a 2 °C min^{-1} heating ramp. For comparison, a pristine ZnO was also prepared in the same procedure without addition of F127.

2.2 Characterisation

X-Ray diffraction (XRD) patterns were obtained on a Philip X'Pert D using Cu-Kα1 radiation at a scan rate of 0.05° 2θ s^{-1} and were used to determine the phase structures of the samples. Transmission electron microscopy (TEM) analysis was conducted using a JEM-2100F microscope (JEOL, Japan) at a 200 kV accelerating voltage. Photocatalyst samples were dispersed in water–methanol and treated with ultrasound for 5 min before deposited on a carbon coated grid.

Brunauer, Emmett, and Teller (BET) surface areas and pore size distribution of the photocatalysts were obtained on Micrometrics Gemini III-2375 (Norcross, GA, USA) instrument by N_2 physisorption at −196 °C. Prior to the measurements, the catalyst was evacuated for 2 h at 150 °C to remove physically adsorbed water. The BET surface area was determined by a multipoint BET method using the adsorption data in the relative pressure (P/P_0) range of 0.05–0.3.

The UV-vis diffuse reflectance spectra were obtained on Perkin Elmer Lambda 950 UV/Vis/NIR spectrophotometer equipped with a 150 mm snap-in integrating sphere for capturing diffuse and specular reflectance. $BaSO_4$ was used as a reflectance standard in the UV-visible diffuse reflectance experiment.

X-Ray photoelectron spectroscopy (XPS) measurements were performed on the ESCALAB-210 spectrometer (Thermo VG Scientific, UK) with an Mg-Kα source. All the binding energies were referenced to the C1s peak at 284.6 eV of the surface adventitious carbon.

2.3 Photocatalytic activity

The photocatalytic activity of the prepared samples in terms of the photocatalytic decolorization of methylene blue (MB) aqueous solution was performed at ambient temperature under visible-light irradiation using a 300 W Xe lamp (15 cm above the dishes) with a 400 nm cutoff filter as a light source.

In the photocatalysis experiments, 0.1 g of the prepared photocatalyst powder was dispersed in a 100 mL MB aqueous solution with a concentration of 10 ppm in a beaker. The mixed solution was remained in dark for an hour to establish an MB solution adsorption–desorption equilibrium on the photocatalyst before light irradiation. During photocatalysis, the 4 mL reaction solution was taken out in every 15 min irradiation interval and filtered to measure the concentration change of MB using a UV-visible spectrophotometer (Scinco, Neosys-2000, South Korea). Since the MB was at rather low concentration in the aqueous solution, its photodegradation followed a pseudo-first-order reaction and its kinetics can be expressed as

$$-\ln(c/c_0) = kt,$$

where k is the apparent rate constant and c_0 and c are the initial and reaction concentrations of aqueous MB solution, respectively.

2.4 Computational details

The density function theory (DFT) calculations of ZnO and C-doped ZnO were performed with the CASTEP package using the generalized gradient approximation (GGA),[25] in the scheme of Perdew–Burke–Ernzerhof (PBE) to describe the exchange–correlation functional. The norm-conserving pseudopotential was adopted rather than ultrasoft pseudopotential because the former is more suitable to simulate the bandgap and optical properties.

For simulating C-doping effects, we first built a $2 \times 2 \times 2$ (32-atom) wurtzite ZnO supercell, containing 16 Zn and 16 O, in which one O atom was replaced by a C atom, corresponding to C doping level of 6.25 at.%. The crystal parameters of wurtzite ZnO unit cell in the DFT calculation are $a = 3.249$ Å and $c = 5.205$ Å. The Monkhorst-Packgrid for SCF calculation is $7 \times 7 \times 4$ with 16 k points was used for integration in the Brillouin zone of the supercell,[26] and the plane-wave kinetic energy cutoff was set to 600 eV. The mechanical equilibrium was achieved through conjugate gradient minimization of the total energy to a tolerance of 2×10^{-6} eV per atom, the maximum forces to a tolerance of 0.05 eV Å^{-1}, and the maximum atomic displacement position tolerance of 1×10^{-3} Å. The $2 \times 2 \times 2$ (32-atom) wurtzite ZnO supercell was also simulated as reference.

3. Results and discussion

3.1 Crystal and textural properties

Fig. 1(a) comparatively shows the XRD patterns of pure and C-doped ZnO samples calcined at 500 °C. All the Bragg diffraction peaks of the ZnO and C-doped ZnO samples can be well indexed according to hexagonal wurtzite ZnO ($P6_3mc$, JCPDS: 890511), though the C-doped ZnO shows weaker diffraction intensity than ZnO, indicating that C-doped ZnO possesses lower crystallinity or smaller crystallite size. The close observation to the strongest peaks (Fig. 1(b)) shows the C-doping leads to (101) diffraction shifting to higher 2θ angle, which is ascribed to doping-induced unit cell deformation. As listed in Table 1, the calculated crystallite size, lattice parameters and unit cell volume of C-doped ZnO are indeed smaller than those of pure ZnO. The C-doping induced ZnO lattice parameters reduction and cell volume shrinking can be
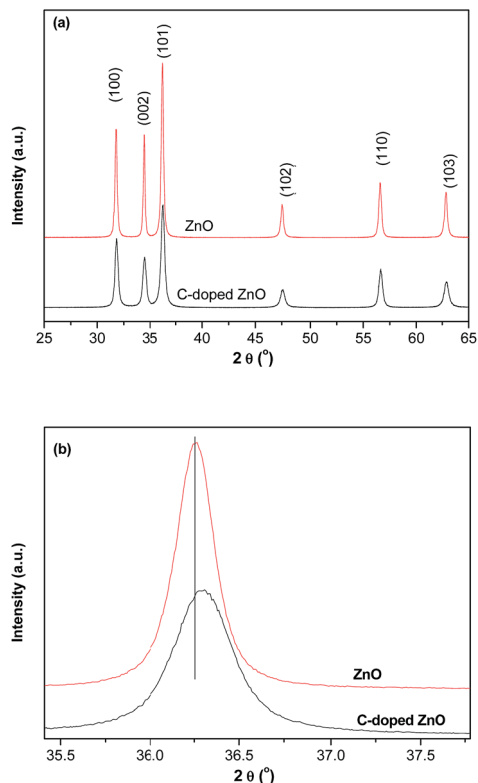
Fig. 1 (a) Full and (b) amplified XRD patterns of the pristine ZnO and C-doped ZnO calcined at 500 °C.

Fig. 2 TEM (ai, bi), HRTEM (aii, bii), lattice fringes (aiii, biii) and SAED (aiv, biv) images of (a) ZnO and (b) C-doped ZnO calcined at 500 °C.

reasonably attributed to structure defects (O_{vac}) caused by C-doping. If there were no O_{vac}, the lattice parameters should have been increased because the carbon anion radius (69–76 pm) is greater than oxygen (57–66 pm). From the charge equilibrium point of view, substitution of O(-II) by C(-IV) would unbalance system charge that requires oxygen loss to remain system neutral. The results agree with previous research where C-doping induced unit cell changes were also observed.[22]

Transmission electron microscope (TEM) was used to further investigate the morphology and crystal structures of ZnO and C-doped ZnO. It can be seen from the TEM images (Fig. 2) that ZnO and C-doped ZnO are in nano-flake morphology (Fig. 2(ai) and (bi)), but C-doped ZnO nanoflakes show more regular hexagonal shape and smaller particle size ($\sim$20 nm) than that of pure ZnO ($\sim$30 nm), which is well consistent with XRD results. The HRTEM images of ZnO and C-doped ZnO are presented in Fig. 2(aii) and (bii), in which the labelled lattice fringes (Fig. 2(aiii) and (biii)) are attributed to d-spacings between adjacent (100) and (101) surfaces,
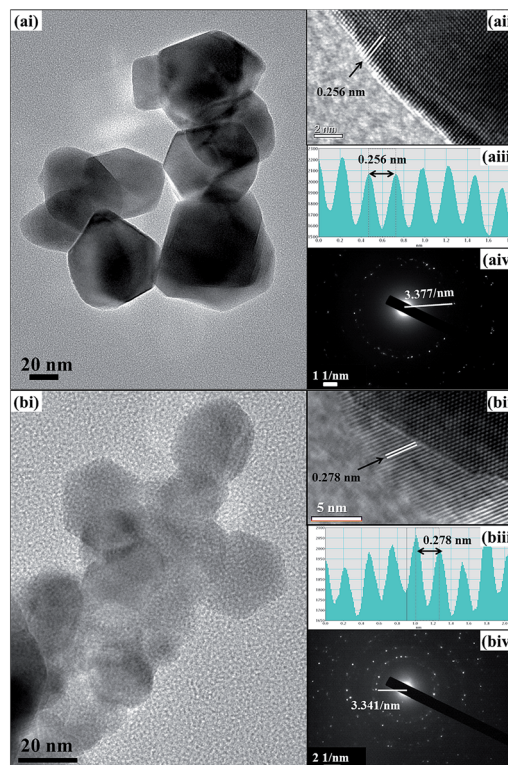
respectively. The angles between the labelled d-spacings are around 45°, corresponding to the dihedral angle between (100) and (101) surfaces. The HRTEM results reveal the largely exposed plane is (001) surface, which is further evidenced by the selected area electron diffraction patterns (SAED, Fig. 2(aiv) and (biv)). The circular multi-spots in the SAED images indicate the samples are polycrystals with (001) surface exposed preferentially.

Polymer surfactants have often used to control morphology and texture of ZnO crystals.[27,28] Large S_{BET} of 12.5 m^2 g^{-1} was ever observed on hierarchical C-doped ZnO prepared *via* a PEG-2000 directed thermal decomposition of $Zn_5(CO_3)_2(OH)_6$ at 500 °C,[7] where the high porosity was attributed to ZnO inter-particle slits and intra-flake voids created by release of volatile gases like CO and H_2O during thermal treatments. However, there were no nano-pores or voids observed on our C-doped ZnO flakes (Fig. 2), which is reasonable since ZnO is easy to crys-tallise before forming regular pores around the polymer template. In our work, polymer surfactant F127 served as both

Table 1 Structural and textural properties of ZnO and C-doped ZnO calcined at 500 °C

| Sample | Crystallite size (nm) | Lattice parameters (Å) | | Unit cell volume (Å^3) | S_{BET} (m^2 g^{-1}) |
		$a = b$	c		
ZnO	27.2	3.2490	5.2061	47.5936	7.1
C-doped ZnO	21.8	3.2448	5.2015	47.4275	17.1

carbon source and pore direct-agent to form ZnO nanoflakes in the C-doped ZnO preparation. The specific surface area (S_{BET}) of the C-doped ZnO is 17.1 m^2 g^{-1} after calcinations at 500 °C (Table 1), approximately 2.5 times that ZnO, and is larger than the hierarchical C-doped ZnO prepared *via* self-doping strategy.[7] The larger S_{BET} of C-doped ZnO is associated with its smaller particle.

3.2 Optical properties

UV-vis diffuse adsorption spectra (UV-DRS) shown in Fig. 3(a) comparatively presents the different light absorption characteristics of pure and C-doped ZnO materials. In comparison with ZnO, C-doped ZnO displays significant red shift of optical bandgap absorption edge into visible-light region as well as enhanced light absorption in the whole UV-visible band. Non-metal doping into wideband metal-oxide photocatalysts, such as N-doped TiO$_2$, may effectively improve their visible-light absorption but at a price to reduce UV absorption.[15,29] Although visible-light absorption is important for C-doped ZnO as a photocatalyst, enhanced UV absorbance would also benefit photocatalysis application of sunlight since UV is more efficient.[14,16] Improvement of UV adsorption of C-doped ZnO is highly dependent on the synthesis strategy and precursors. For instance, enhanced UV adsorption was ever observed on C-doped ZnO photocatalyst derived from zinc gluconate precursor,[14] but C-doped ZnO synthesised *via* Vitamine C or self-doping strategies did not show improved adsorption of UV light.[7,8]
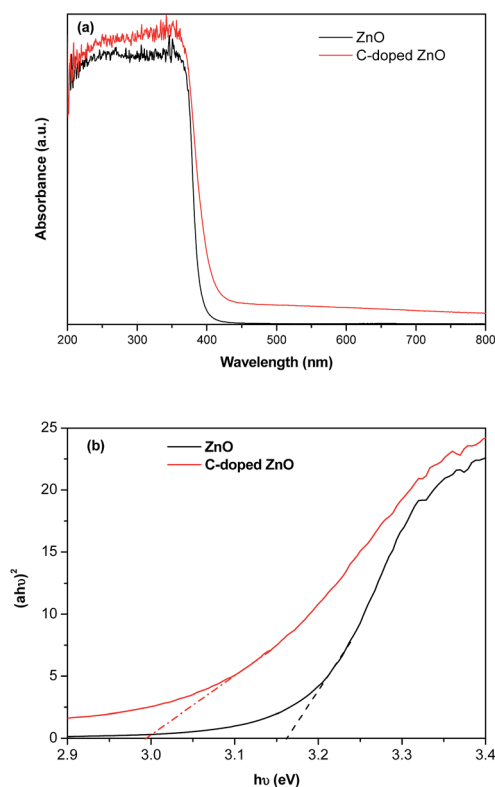
Applying Kubelka–Munk rule the direct bandgap energies of ZnO (3.17 eV) and C-doped (2.98 eV) ZnO may be extracted precisely from their $(ah\nu)^2$ *vs.* $h\nu$ plots as shown in Fig. 3(b). More importantly, the $(ah\nu)^2$ *vs.* $h\nu$ plot in bandgap region for C-doped ZnO is linear similar to that of ZnO, revealing the C-doping did not change direct electron transition characteristic of ZnO in badgap.[7] Enhanced light harvesting and direct transition characteristics are highly desirable for doped ZnO materials in photocatalysis, opticoelectronic and solar cell applications.

Like ZnO, the disrupt drop of light-absorption in bandgap region of C-doped ZnO is observed clearly, suggesting that carbon was incorporated into ZnO matrix rather than laid down on ZnO surface. The C in ZnO lattice would revise ZnO's band structure to introduce impurity midgap(s) and thus tune its bandgap. Besides bandgap light absorption, visible-light absorption on the C-doped ZnO is also tailed beyond 800 nm which is a typical red shift induced by impurity adsorption or oxygen-vacancies (O$_{vac}$).[15,23] Advanced characterisations are necessary to determine C-species and O$_{vac}$ for understanding the nature of visible-light response on the C-doped ZnO.

3.3 Surface component and electron structure

3.3.1 XPS analysis. XPS measurements were conducted to analyse surface species and valence band of both ZnO and C-doped ZnO so as to understand the origin of visible-light response of C-doped ZnO. Fig. 4(a)–(d) present the acquired C1s, O1s and Zn 2p core level as well as the valence-band XPS spectra of pure and C-doped ZnO calcined at 500 °C, which clearly distinguished the differences between ZnO and C-doped ZnO in both core level and valance electron bands.

As shown in Fig. 4(a), two sets of peaks are observed in the C1s XPS spectra for both pure and C-doped ZnO samples, including a large peak with binding energy (BE) ranging from 282 to 286.5 eV and a satellite peaks at higher BE region. With the same BE centring at 288.7 eV, the satellite peaks for pure and C-doped ZnO samples are attributed to the adsorbed CO$_2$ and structural carbonate species containing C=O.[7,13] Such species containing C=O was ever predicted by DFT calculation and evidenced experimentally for C-anion-doped TiO$_2$,[18,19] whereas the C1s satellite peak is broader, revealing a portion of such C species would be from carbonate species trapped in C-doped ZnO matrix or existing incompletely decomposed carbonate precursors.[7]

The major C1s XPS peak of C-doped ZnO is asymmetric and distinct from that of ZnO. The main peak centres at 284.6 eV for ZnO is symmetric and can be ascribed to adventitious hydrocarbon. However, the asymmetric major peak of C1s XPS for C-doped ZnO centres at 284.4 eV, 0.2 eV red-shift relative to that in ZnO, which is resulting from peaks overlap between contaminant carbon and other carbon species. The major C1s XPS peak was therefore fitted into 4 peaks: the largest one at 284.6 eV can be assigned to adventitious hydrocarbon, while 286.2 eV and 283.8 eV are due to Zn–O–C and Zn–C bonds,[22] respectively. The smallest fitted peak at 282.9 eV is associated to Zn–C bond connected with oxygen-vacancy (O$_{vac}$) since additional electron density would be imposed from negative-

Fig. 3 UV-vis diffuse adsorption spectra (a) and corresponding $(ah\nu)^2$ *vs.* $h\nu$ plots for (b) ZnO and C-doped ZnO calcined at 500 °C.
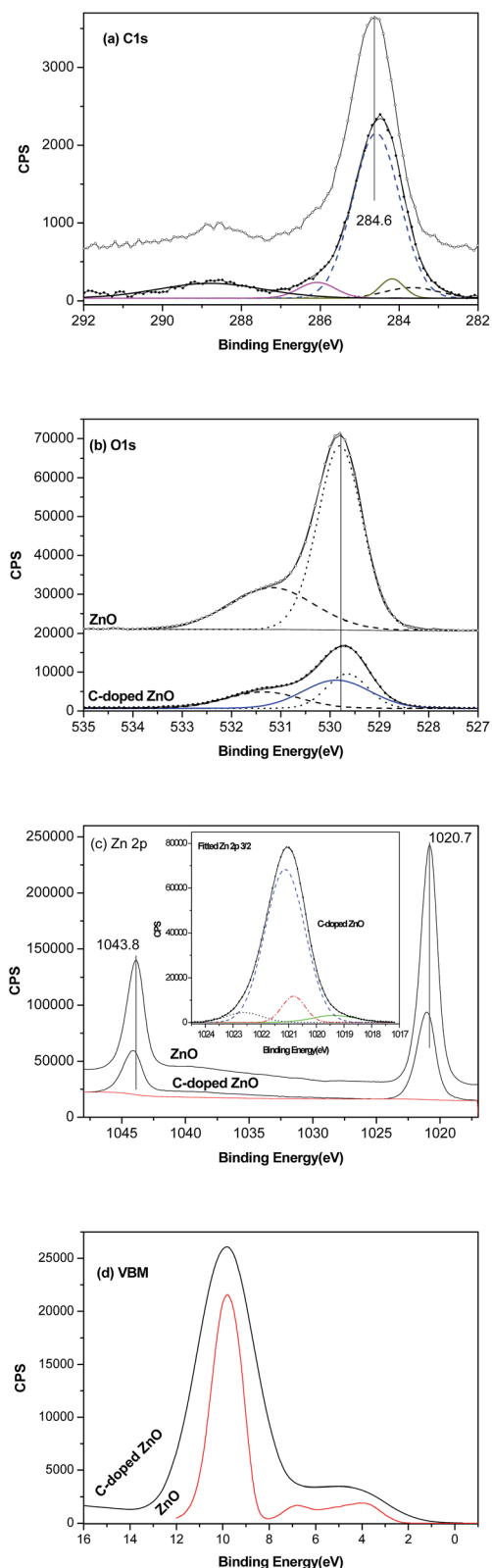
Fig. 4 Core level XPS spectra of (a) C1s, (b) O1s, (c) Zn 2p and (d) valence band in ZnO and C-doped ZnO photocatalysts calcined at 500 °C.

charged O_{vac} onto C in the Zn–C–O_{vac} bond. It has been well accepted that O_{vac} may result in bandgap narrowing,[23] therefore it is necessary to address the contributions of Zn–C and O_{vac} to the visible-light response of C-doped ZnO.

The areas of C1s XPS peaks due to Zn–O–C, Zn–C and Zn–C–O_{vac} are almost the same. In principle, zinc carbonate species would not cause visible light response in ZnO,[7] hence, it can be concluded the visible-light-response should be associated directly with Zn–C species and Zn–C–O_{vac} induced by carbon-doping. As discussed in UV-vis-DRS, O_{vac} would mainly be responsible for the light response in the whole visible-light range that accounts for grey colour of our C-doped ZnO, but also influences bandgap adsorption as discussed in electronic structure section.

Fig. 4(b) presents the O1s XPS of pure and C-doped ZnO calcined at 500 °C. For pure ZnO, a large O1s locates at 529.8 eV is due to Zn–O bonds in wurtzite ZnO crystal, and a shoulder peak (531.3 eV) of 25% height to the major peak may be due to surface chemical adsorbed oxygen species, such as OH⁻ group and carbonates.[22] The O1s XPS of C-doped ZnO encompasses a major peak at 529.7 eV along with a shoulder peak (531.5 eV) of 33% intensity to the major peak, suggesting the O1s components locates in different environment from those in ZnO. O1s XPS of C-doped ZnO were fitted into 3 peaks centring at 531.5, 529.9 and 529.7 eV. The peak at 531.5 eV may be ascribed to surface adsorbed oxygen species (OH group) and carbonate species (i.e. C–O and C=O bonds). The peak at 529.6 eV is assigned to O^{2-} ions of Zn–O bonds in Wurtzite structure with Zn^{2+} in hexagonal coordinations, and O1s peak at 529.9 eV can be reasonably attributed to Zn–O_{vac} and Zn–O–C bonds because C-dopant and O_{vac} usually induce blue shift of Zn–O bond.[23] It is difficult to determine the concentrations of O_{vac} and Zn–C–O or Zn–O–C species from O1s XPS because the peaks are heavily overlapped.

Fig. 4(c) compares the Zn 2p XPS spectra of ZnO and C-doped ZnO. It can be clearly seen that the Zn $2p_{3/2}$ and $2p_{5/2}$ XPS lines in C-doped ZnO are blue shifted (0.2 eV) systematically relative to pure ZnO. The BE difference between Zn $2p_{3/2}$ and $2p_{5/2}$ XPS lines remains 23.1 eV for ZnO and C-doped ZnO, suggesting Zn is in Zn^{2+} state for the two samples.[22] The Zn $2p_{3/2}$ state was further fitted into 4 peaks (inserted in Fig. 4(c)) corresponding to Zn–C (1019.3, 4.3%), Zn–O–C (1020.8 eV, 8.2%), Zn–O (1021.1 eV, 82.6%) and Zn–O_{vac} (1022.6 eV, 4.9%) bonds, respectively. The results reveal the carbon concentration is around 12.5 atm% relative to Zn, 2.5 times that O_{vac} concentration. However, the concentration of Zn–C carbide species is nearly equal to that of O_{vac}, suggesting the formation of each Zn–C bond would create at least one O_{vac} site which agrees with the C1s XPS analysis.

Valence band (VB) XPS is a powerful tool to investigate the influence of impurity on the band structure of semiconductors. Fig. 4(d) comparatively shows VB XPS spectra acquired on ZnO and C-doped ZnO. It clearly shows the C-doping not only red-shifts valance band maximum (VBM) energy but also expands the VB band width. The VBM of ZnO is approximately 2.24 eV relative to vacuum level yet lifts up to 1.33 eV once doped with carbon, revealing C-doping in this case is an n-type doping. In

addition, the ZnO VB with width about 6.0 eV is more localised with clear discrete energy levels than the VB of C-doped ZnO. The VB width of C-doped ZnO is greater than 7.0 eV and over-lapped with deeper energy level, revealing its VB electrons are delocalised and more dispersive.

3.3.2 Electronic structure. CASTEP code was used to simulate the electron structures of wurtzite ZnO and C-doped ZnO crystals. Fig. 5(a) and (b) compares the simulated band structures of ZnO and C-doped ZnO, showing C-doped ZnO possesses much higher electron density of state (DOS) because of C-doping induced electron delocalisation. A new electron density of sate at ~10 eV due to C 2s state is also observed in the C-doped ZnO. The calculated E_g of ZnO is 0.97 eV, which is much smaller than experimental value (3.17 eV) due to the choice of GGA exchange–correlation energy in DFT simulation. However, it is fairly larger than E_g calculated using ultrasoft pseudopotential,[7] indicating the advantage of norm-conserving pseudopotential over ultrasoft pseudopotential in band structure simulation. Simulation using GGA + U function may predict E_g closer to experimental value while it is rather expensive since it estimates E_g based on GGA geometry optimisation.[17,18] Within our approximation, GGA modelling provided here sufficient accuracy for the influence of C-dopant on the VB position and C donor states relative to the VBM.

The calculated VB width is approximately 5.5 and 6.1 eV for ZnO and C-doped ZnO, respectively, which are well consistent with the VB XPS results. In addition, the conductance band minimum (CBM) was dropped down around 1.0 eV compared to ZnO. The valance band maximum (VBM) and conductance band minimum (CBM) of the pure and C-doped ZnO are both locating at G points, indicating their direct electron transition in bandgap region that are convined by the experimental UV-vis-DRS characterisation results (Fig. 3(b)). The VBM of C-doped ZnO joints with its CBM at G point leading to vanishing of bandgap of C-doped ZnO, which is mainly due to a new additional C 2p state on top of O 2p state of ZnO (Fig. 7(c) and S1a†) and the underestimated E_g.

The enhanced DOS, narrowed bandgap and extended bandwidth of C-doped ZnO relative to ZnO are further detailed by the PDOS plots shown in Fig. 6(a) and (b). It can be seen the VB of ZnO is mainly composed of p state electrons well dispersed in the whole VB region as well as the s and d states appearing at slightly deeper VB band. The major component of ZnO valance band maximum (VBM) is p state and involves a small amount of d state electrons. The conductance band minimum (CBM) of ZnO is only containing s state electrons. In contrast, the VB of C-doped ZnO is mainly composed of p state electrons but the s and d state electrons also contributed significantly to its VBM. It is notable that the CBM of C-doped ZnO contains s and p state electrons.

Combined Fig. 6 and the element PDOS results presented in Fig. 7(a–c) and S1(a,b),† it can be concluded that the VB of ZnO is composed of hybridised O 2p and Zn 3d states, and its CB comprises of Zn 4s states and O 2p at higher energy level. From the Zn and O PDOS plots in Fig. S1,† it may be found ZnO VBM is mainly composed of O2p sates hybridising with a little Zn 3d
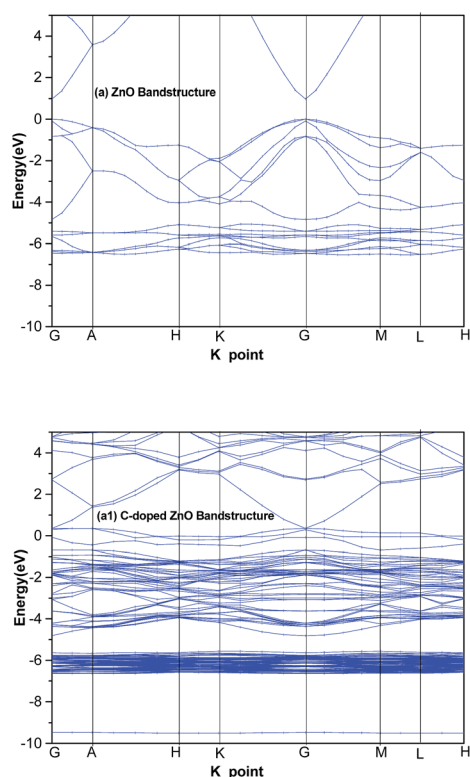

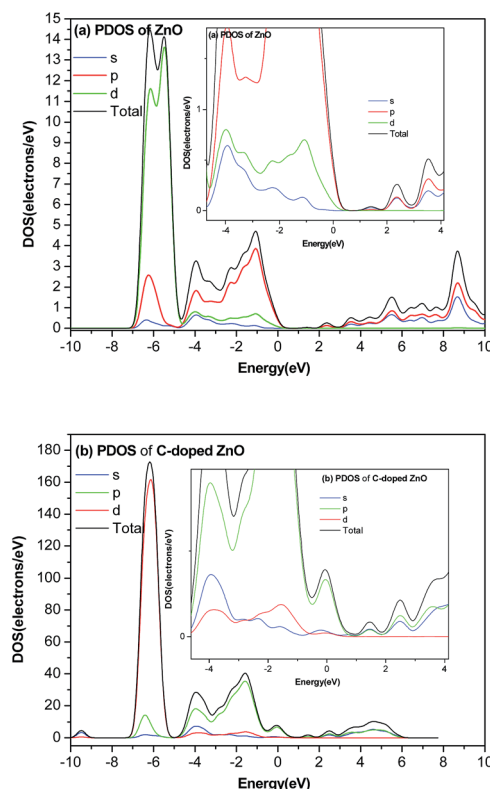Fig. 5 Simulated band structures of Wurtzite (a) ZnO and (b) C-doped ZnO.

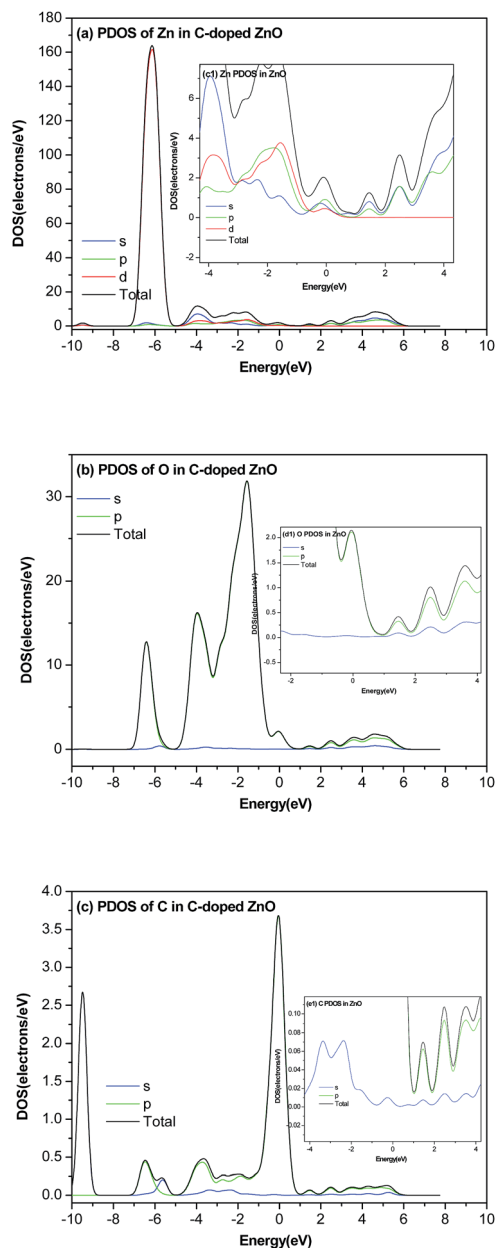Fig. 6 PDOS of Wurtzite structured (a) ZnO and (b) C-doped ZnO crystals.

Fig. 7 PDOS of Zn (a), O (b) and C (c) of C-doped ZnO Wurtzite crystal. Insets correspond to amplified PDOS around bandgap region.

state, while Zn 4s state dominates the CBM. Once C is incorporated into ZnO, new electron states are appeared at VBM and pinned at Fermi level. The VBM are occupied by C 2p state (Fig. 7(c)) with hybridised Zn 3d and 4 s states (Fig. 7(a) and (b) and insets). The CBM of C-doped ZnO is dominated by s state with almost equal amount of p state. Apparently, the VBM and CBM components of C-doped ZnO distinctly distinguish from those of ZnO and its reduced bandgap is mainly due to new states arisen from C-doping. The components of CBM in C-doped ZnO are also changed correspondingly in comparison to ZnO.

It is essential to further quantitatively investigate the components of the new additional states on top of VBM and CBM which

disclose the roles of C-doping in narrowing bandgap of C-doped ZnO. As shown in Fig. 7(a–c), the detailed PDOS of Zn, O and C in C-doped ZnO verify its VBM state are mainly composed of C 2p sate ($\sim$50%), O 2p ($\sim$25%) and hybridised 4s and 3d states (25%) of Zn. The new O and Zn states at VBM can be attributed to oxygen vacancies induced by C-doping so as to remain the overall charge neutrality after substitution of O^{2-} by C^{4-} in ZnO matrix.[18] Although Zn 4s state dominates CBM of C-doped ZnO, O 2p and 2s states also contribute around 25% CBM while the contribution of C-dopant (2p state) to the CBM is negligible.

Combining the experimental VBM XPS and theoretical PDOS analyses we can now draw an elusive scheme of band structure of C-doped ZnO as shown in Fig. 8, which clearly shows the bandgap narrowing of C-doped ZnO is mainly induced by C-doping and derived O_{vac}: the new states of C 2p and O_{vac}-related O 2p, Zn 3d and 4s lift up VBM of ZnO; the Zn 4s and O 2p states of O_{vac} comprise of the CBM in C-doped ZnO which pushes the CBM down to lower energy level. In all, it is the additional energy levels induced by C-doping and O_{vac} narrowing the bandgap of C-doped ZnO in comparison to ZnO.

3.4 Photocatalytic activity

Fig. 9(a) shows the time-dependent absorbance spectra of MB on C-doped ZnO under visible light illumination, revealing the gradual decolourisation of MB on C-doped ZnO under visible light irradiation. The photodegradation should be induced by the photocatalytic reaction because MB degradation is negligible without photocatalyst and no degradation was observed on the photocatalysts in dark. Despite the fact that C-doped ZnO possessed enhanced light absorption, ZnO exhibited notably higher photoactivity in MB degradation than C-doped ZnO under visible light irradiation (Fig. 9(b)). It is well known that photocatalysis follows the first order kinetics law, so that the apparent reaction kinetics constant, k, can be extracted from the slope of plot of $-\ln(c/c_0)$ vs. reaction time.[7,14,15] The calculated k values for ZnO and C-doped ZnO are 0.009 and 0.006 min^{-1}, respectively. ZnO possesses better activity and larger k_{ZnO} than C-doped ZnO, suggesting the visible-light-driven MB photodecomposition should not be dominated by bandgap excitation.

Owing to the wide bandgap, valence band electrons of ZnO cannot be excited by visible light so that MB photodegradation
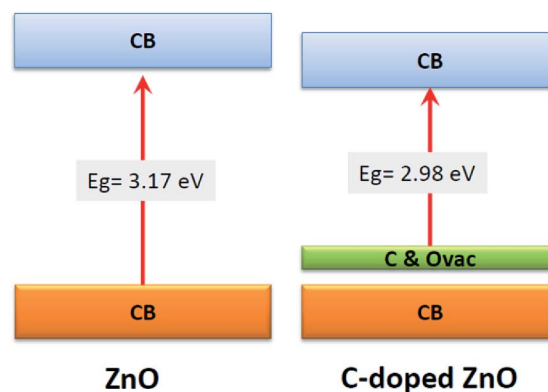

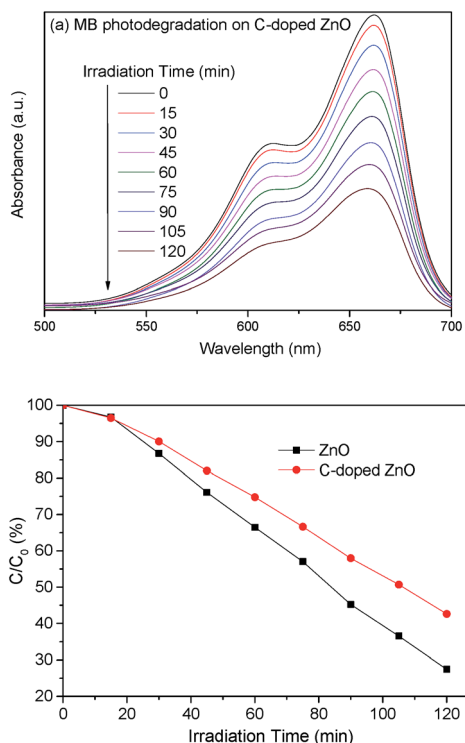Fig. 8 Schematic band structures of ZnO and C-doped ZnO crystals.

Fig. 9 (a) UV-vis spectra on C-doped ZnO and (b) photocatalytic activity on ZnO and C-doped ZnO for Methylene degradation.

on ZnO is attributed to dye-sensitised photocatalysis. Under visible light illumination MB is excited by light of wavelength shorter than its characteristic absorption wavelength (662 nm) and then injects photoexcited electrons into ZnO conduction band (CB). The electrons injected onto ZnO CB react with dissolved oxygen and give rise to active oxygen species which can decompose the excited MB.[7,14] In contrast, C-doped ZnO may be excited by visible light due to its narrowed bandgap to lift valence electrons onto CB and leave holes on VB. Furthermore, C-doped ZnO should have been shown stronger dye-sensitising effect than ZnO since C-doped ZnO possesses larger S_{BET} and thus sensitising opportunity due to higher MB adsorption amount. It seemed the heavy C-doped ZnO should be more active, whereas the experimental results showed it is less active than ZnO, suggesting heavy C-doping would deteriorate the dye-sensitised photodegradation. It is reasonable to conclude that bandgap excitation of the C-doped ZnO contributes a little to the overall MB photodegradation in comparison to dye-sensitisation under visible-light illumination. The fact is that heavy C-doping and derived O_{vac} correspondingly would serve as recombination centres in the photoreaction which reduce dye-sensitising effects by trapping the electrons from excited dyes and thus deteriorate photodegradation on C-doped ZnO relative to ZnO.

In general, the enhanced light absorption corresponds to enhanced photoexcitation while the photo excitons are prone to recombination leading to almost 95% loss of absorbed light energy.[4,5,24] The charge recombination centres may be overloaded dopants or structure deficiencies, for instance O_{vac}.

Previous report evidenced there exists optimum C-doping range for promoting visible-light-driven photoreactivity while photocatalytic activity would be lower beyond the suitable C-doping levels.[7] C-doped ZnO containing 2.7 at.% C showed higher activity than that containing 0.41 at.% C-dopant.[8] However, the roles of O_{vac} were not paid enough attention. We did find the photocatalytic activity may be improved for light-C-doped ZnO prepared through reducing F127 amount (ESI, Fig. S2†), while this research focused on the heavy C-doping sample because it is more important to unveil the function of coexistence of C^{4-} and O_{vac}. Despite the fact that suitable amount of O_{vac} can extend light absorption into visible light region and improve photocatalytic activity, the photoreactivity will drop dramatically if O_{vac} concentration is greater than certain amount.[15,23] In this research, the C-doping level is quite high with almost 4.3 at.% carbide-based C^{4-} coexisting with comparable amount of O_{vac} in the C-doped ZnO. Hence, the low visible-light-driven photocatalytic activity on the C-doped ZnO was tentatively assigned to the synergistic consequences of the overloaded C-dopants and O_{vac} that favour the recombination of photogenerated charge carriers under irradiation.

4. Conclusion

C-doped ZnO nanoflakes with large surface area were successfully synthesised *via* a pyrolysis process using Pluronic F127 as polymer-directed agent. The C-doping leads to enhanced UV and visible light absorption yet does not affect the electron (direct) transition characteristic of ZnO. The direct bandgap of the C-doped ZnO is 2.98 eV though its light adsorption tails beyond visible light region because of co-existing oxygen vacancies and C-dopants.

VBM XPS evidenced the C-doping expends VB width of ZnO and lifts its VBM energy as well as draws the CBM down towards Fermi level, leading to narrowed bandgap. DFT simulations reveal the origin of visible-light-response of C-doped ZnO is also related to additional bandgap electron states (midgap energy levels) arisen from C-doping and correspondingly created O_{vac} stemmed from C-doping. Distinguished from O2p and Zn 4s states composing ZnO VBM and CBM, the VBM of C-doped ZnO is dominated with C2p state and its CBM mainly contains Zn 4s along with additional states of Zn 3d and hybridised states of O 2s and O2p of O_{vac}. Although the C-doped ZnO showed enhanced light absorption, its visible-light-driven activity in MB photodegradation is worse than that ZnO because the C-doping and corresponding O_{vac} led to significant charge recombination.

Acknowledgements

References

1 A. Kubacka, M. Fernández-García and G. Colón, *Chem. Rev.*, 2011, **112**, 1555–1614.

2 R. E. Galian and J. Perez-Prieto, *Energy Environ. Sci.*, 2010, **3**, 1488–1498.

3 Y. Tachibana, L. Vayssieres and J. R. Durrant, *Nat. Photonics*, 2012, **6**, 511–518.

4 A. Ajmal, I. Majeed, R. N. Malik, H. Idriss and M. A. Nadeem, *RSC Adv.*, 2014, **4**, 37003–37026.

5 M. Pelaez, N. T. Nolan, S. C. Pillai, M. K. Seery, P. Falaras, A. G. Kontos, P. S. M. Dunlop, J. W. J. Hamilton, J. A. Byrne, K. O'Shea, M. H. Entezari and D. D. Dionysiou, *Appl. Catal., B*, 2012, **125**, 331–349.

6 M. N. Chong, B. Jin, C. W. K. Chow and C. Saint, *Water Res.*, 2010, **44**, 2997–3027.

7 S. Liu, C. Li, J. Yu and Q. Xiang, *CrystEngComm*, 2011, **13**, 2533–2541.

8 S. Cho, J.-W. Jang, J. S. Lee and K.-H. Lee, *CrystEngComm*, 2010, **12**, 3929–3935.

9 Y.-G. Lin, Y.-K. Hsu, Y.-C. Chen, L.-C. Chen, S.-Y. Chen and K.-H. Chen, *Nanoscale*, 2012, **4**, 6515–6519.

10 S.-M. Lam, J.-C. Sin, A. Z. Abdullah and A. R. Mohamed, *Desalin. Water Treat.*, 2012, **41**, 131–169.

11 F. Wang, L. Liang, L. Shi, M. Liu and J. Sun, *Dalton Trans.*, 2014, **43**, 16441–16449.

12 D. Chen, Z. Wang, T. Ren, H. Ding, W. Yao, R. Zong and Y. Zhu, *J. Phys. Chem. C*, 2014, **118**, 15300–15307.

13 H. Pan, J. Yi, L. Shen, R. Wu, J. Yang, J. Lin, Y. Feng, J. Ding, L. Van and J. Yin, *Phys. Rev. Lett.*, 2007, **99**, 127201.

14 O. Haibo, H. J. Feng, L. Cuiyan, C. Liyun and F. Jie, *Mater. Lett.*, 2013, **111**, 217–220.

15 Z. Jiang, L. Kong, F. S. Alenazey, Y. Qian, L. France, T. Xiao and P. P. Edwards, *Nanoscale*, 2013, **5**, 5396–5402.

16 S. U. M. Khan, M. Al-Shahry and W. B. Ingler, *Science*, 2002, **297**, 2243–2245.

17 K. Yang, Y. Dai, B. Huang and M.-H. Whangbo, *Chem. Mater.*, 2008, **20**, 6528–6534.

18 K. Yang, Y. Dai, B. Huang and M.-H. Whangbo, *J. Phys. Chem. C*, 2009, **113**, 2624–2629.

19 W. Ren, Z. Ai, F. Jia, L. Zhang, X. Fan and Z. Zou, *Appl. Catal., B*, 2007, **69**, 138–144.

20 D. E. Zhang, M. Y. Wang, J. J. Ma, G. Q. Han, S. A. Li, H. Zhao, B. Y. Zhao and Z. W. Tong, *Funct. Mater. Lett.*, 2014, **07**, 1450026.

21 S. T. Tan, X. W. Sun, Z. G. Yu, P. Wu, G. Q. Lo and D. L. Kwong, *Appl. Phys. Lett.*, 2007, **91**, 072101.

22 D. K. Mishra, J. Mohapatra, M. K. Sharma, R. Chattarjee, S. K. Singh, S. Varma, S. N. Behera, S. K. Nayak and P. Entel, *J. Magn. Magn. Mater.*, 2013, **329**, 146–152.

23 J. Wang, Z. Wang, B. Huang, Y. Ma, Y. Liu, X. Qin, X. Zhang and Y. Dai, *ACS Appl. Mater. Interfaces*, 2012, **4**, 4024–4030.

24 S. G. Kumar and K. S. R. K. Rao, *RSC Adv.*, 2015, **5**, 3306–3351.

25 J. P. Perdew, K. Burke and M. Ernzerhof, *Phys. Rev. Lett.*, 1997, **78**, 1396.

26 H. J. Monkhorst and J. D. Pack, *Phys. Rev. B: Condens. Matter Mater. Phys.*, 1976, **13**, 5188–5192.

27 A. Bagabas, A. Alshammari, M. Aboud and H. Kosslick, *Nanoscale Res. Lett.*, 2013, **8**, 516.

28 H. Li, Y. Zhang and J. Wang, *J. Am. Ceram. Soc.*, 2012, **95**, 1241–1246.

29 R. Asahi, T. Morikawa, T. Ohwaki, K. Aoki and Y. Taga, *Science*, 2001, **293**, 269–271.